THE JOURNAL OF PHYSICAL CHEMISTRY C

Article

pubs.acs.org/JPCC

Ultrasmall MgH_2 Nanoparticles Embedded in an Ordered Microporous Carbon Exhibiting Rapid Hydrogen Sorption Kinetics

Claudia Zlotea,*[,†] Yassine Oumellal,[†] Son-Jong Hwang,[‡] Camelia Matei Ghimbeu,[§] Petra E. de Jongh,[∥] and Michel Latroche[†]

[†]Institut de Chimie et des Matériaux Paris-Est, UMR 7182 CNRS-UPEC, 2-8 rue Henri Dunant, 94320 Thiais, France

[‡]Division of Chemistry and Chemical Engineering, California Institute of Technology, Pasadena, California 91125, United States

[§]Institut de Science des Matériaux de Mulhouse, UMR 7361 CNRS-UHA, 15 rue Jean Starcky, 68057 Mulhouse, France

[∥]Inorganic Chemistry and Catalysis, Debye Institute for Nanomaterials Science, Utrecht University, Universiteitsweg 99, 3584 CG Utrecht, The Netherlands

Supporting Information

ABSTRACT: MgH_2 nanoparticles with different average sizes have been prepared as ordered microporous carbon by tuning the Mg amount from 15 to 50 wt %. Ultrasmall particles with mean sizes of 1.3 and 3.0 nm have been obtained for 15 and 25 wt % Mg contents, respectively. The hydrogen desorption properties strongly depend on the nanoparticle size, as evidenced by different thermal analysis techniques. The onset temperature of hydrogen desorption for MgH_2 nanoparticles below 3 nm occurs at a temperature about 245 K lower than for microcrystalline material. Two distinct hydrogen desorption peaks are noticed for nanoparticles with mean sizes of 1.3 and 3.0 nm, as confirmed by TDS and HP-DSC. ^{1}H NMR investigations suggest the presence of two MgH_2 populations with enhanced hydrogen mobility, as compared to the microcrystalline hydride. The short hydrogen diffusion path and the enhanced hydrogen mobility may explain the increased desorption kinetics of these ultrasmall nanoparticles.

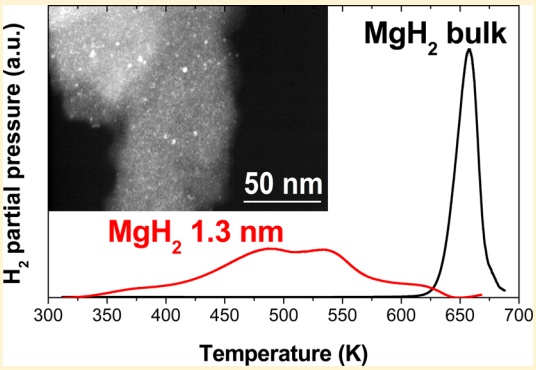

INTRODUCTION

As compared to the bulk state, nanostructured materials offer larger surface-to-volume ratios, faster transport properties, altered physical properties, and interesting confinement effects that are consequences of the combination of their nanoscale dimensions and interaction with the supports. Due to these exciting properties, nanomaterials have been extensively studied for energy-related applications such as catalysis, solar cells, thermoelectrics, supercapacitors, batteries, and solid-state hydrogen storage systems.[1,2] In this context, remarkable research efforts have been made worldwide to develop safe, compact, and efficient solid-state storage devices for hydrogen.

Among many metals and alloys that can reversibly react with hydrogen, Mg shows great promise since it is nontoxic and abundant in the earth's crust, and the related dihydride (MgH_2) possesses high volumetric (110 $g{\cdot}L^{-1}$) and gravimetric capacities (7.6 wt %). However, Mg has unfavorable thermodynamic properties (high stability that requires the use of high temperature to deliver 0.1 MPa hydrogen) and slow reaction kinetics with hydrogen for applications in practical devices. Theoretical calculations have predicted a reduction of the thermodynamic stability of MgH_2 by downsizing to 1.3 nm (nanosizing)[3,4] and by steric stabilization of such very small particles through embedding into porous scaffolds (nanoconfinement).[5] Indeed, confined Mg-based nanoparticles in different scaffolds have been demonstrated to improve hydrogen sorption properties, as frequently reported in the recent literature.[6−13] However, only modest modifications of thermodynamic equilibrium have been reported by nanosizing/nanoconfinement since the least-positive value of the enthalpy of desorption is counteracted by the least-positive entropy change.[10] Therefore, the reported thermodynamic changes correspond to a decrease in the equilibrium temperature for delivering 0.1 MPa hydrogen by 6 and 11 K for ∼7 and 3 nm MgH_2 nanoparticles, respectively, as compared to microcrystalline MgH_2.[10,14]

The main progress obtained by nanosizing/nanoconfinement concerns the significant change in the absorption/desorption reaction kinetics.[10,11,15] The maximum hydrogen desorption rate of MgH_2 nanoparticles with average sizes in the range of 5−20 nm occurs at a 140−150 K lower temperature, as compared to that of the bulk.[11,16] Moreover, the capacity of nanoconfined MgH_2 during hydrogenation/dehydrogenation cycling shows rather good stability.[11,17] Despite these positive

Received: June 16, 2015
Revised: July 10, 2015
Published: July 21, 2015

DOI: 10.1021/acs.jpcc.5b05754
J. Phys. Chem. C 2015, 119, 18091−18098

effects, the desorption kinetics can sometimes become slower upon cycling,[11] suggesting particle agglomeration/recrystallization during cycling as recently proven by in situ synchrotron diffraction experiments.[18]

Nanosizing/nanoconfinement effects have been examined for MgH_2 nanoparticles with sizes of 5−20 nm.[7,9,11,15,16] To the best of our knowledge, only two previous studies have dealt with ultrasmall MgH_2 nanoparticles (<3 nm) embedded in a microporous carbon scaffold.[10,19] Vajeeston et al. have shown from small-angle neutron scattering experiments that it is possible to nanoconfine MgD_2 in activated carbon fibers without further investigation of their hydrogen sorption measurements.[19] Zhao-Karger et al. have reported hydrogen sorption properties of MgH_2 nanoparticles with a size of ∼3 nm.[10] However, the hydrogen sorption properties of ultrasmall MgH_2 nanoparticles (∼1 nm) have never been reported because of a challenging synthesis method and their extremely high reactivity to air.

The present study reports on the synthesis and hydrogen sorption properties of MgH_2 nanoparticles with average sizes of 1.3, 3.0, and ca. 20 nm confined/supported into an ordered microporous carbon template (average pore size of around 1.3 nm). The average particle size depends on the amount of metal inserted into the carbon. For low metal content, ultrasmall MgH_2 nanoparticles of 1.3 nm are formed, whereas for higher metal content the size of the nanoparticles grows accordingly. The present report highlights the importance of size effects on the hydrogen desorption properties of nanoconfined MgH_2. Moreover, ^{1}H NMR investigations confirm the higher hydrogen mobility within nanoparticles relative to that of microcrystalline MgH_2.

EXPERIMENTAL DETAILS

Synthesis of Materials. The ordered microporous carbon material used in this study has been prepared by a hard-template method starting from zeolite β, 930NHA (Tosoh Corporation), as described in previous publications.[20−22] The zeolite pores were filled with propylene by a CVD process at 973 K for 3 h, followed by a thermal treatment in Ar at 1173 K for 3 h to improve the textural and structural properties of the carbon. The zeolite template was eliminated by etching with concentrated HF aqueous solution (40 vol %) and subsequently with HCl solution (37 vol %). The final carbon material (CT) was obtained by washing the residue with water and then subsequent drying. The ordered carbon is microporous with a specific surface area of 2344 $m^2 \cdot g^{-1}$ and a mean pore size of ∼1.3 nm (Figure SI-1). Supplementary details of the carbon physicochemical characteristics can be found elsewhere.[22]

The MgH_2@CT composites have been prepared by so-called bottom-up method.[11,23] Briefly, CT is impregnated with a commercial solution of $MgBu_2$ (Sigma-Aldrich). After solvent removal by evaporation, the precursor is hydrogenated inside an airtight sample holder under 5 MPa H_2 pressure at 423 K for 12 h. The hydrogenation reaction was monitored by high-pressure differential scanning calorimetry during constant heating to 473 K (5 $K \cdot min^{-1}$) under 2.4 MPa H_2 (Figure SI-2). An exothermic peak is noticed at 408 K which corresponds to the hydrogenation of the $MgBu_2$ precursor (Bu_2Mg@C + H_2 → MgH_2@C + $2C_4H_{10}\uparrow$). The reaction produces MgH_2 nanoparticles distributed homogeneously over the carbon scaffold, as already demonstrated.[11,15] Three composites are synthesized with the following loadings: 15, 25, and 50 wt % Mg. The samples are further named $x$$MgH_2$@CT, where x stands for the wt % values. These materials are extremely reactive to air and moisture, so we stored and handled them inside a purified Ar glovebox.

Characterization. *X-ray Powder Diffraction.* The structural properties of the composites have been characterized by X-ray powder diffraction (XRD) using a D8 Advance Bruker diffractometer (CuKα radiation and Bragg−Brentano geometry). All XRD measurements have been performed under an Ar atmosphere using an airtight sample holder. Experimental XRD patterns have been analyzed with TOPAS software (Bruker AXS Topas 4.2) to obtain the lattice parameter from the position of the diffraction peaks and the crystallite size by line-profile fitting using the fundamental parameters approach (if applicable).[24]

Microstructural Measurements. Microstructural observations were performed by transmission electron microscopy (TEM) with a 200 kV FEG TEM (FEI Tecnai F20, point resolution 0.24 nm). The composites have been transferred under Ar directly into the microscope by using an airtight sample holder. All measurements have been performed at 110 K to avoid sample decomposition by beam irradiation. MgH_2 particle size distributions and average sizes have been determined by statistical analyses of several TEM images.

Textural Properties. The textural properties have been determined by nitrogen adsorption isotherm at 77 K using an Autosorb IQ Quantachrome instrument. The samples have been loaded inside an Ar glovebox and transferred to the instrument under a protective atmosphere. Prior to measurements, the samples have been degassed under vacuum at 473 K for 12 h. The specific surface area was obtained by the BET method in the relative pressure range (P/P_0) of 0.02−0.15, and the total pore volume was computed from the amount of gas adsorbed at P/P_0 = 0.97. The microporous volume was calculated using the Dubinin−Radushkevich (DR) equation in the relative pressure range of 10^{-4}−10^{-2}, and the mesoporous volume was determined as the difference between the total and micropore volumes.[25]

Thermal Desorption Spectroscopy. The hydrogen desorption properties have been studied by thermal desorption spectroscopy (TDS) using a homemade instrument detailed in a previous report.[11] The samples were loaded without air exposure, and the H_2 partial pressure was recorded while applying a constant temperature rate of 1 $K \cdot min^{-1}$ from 300 to 700 K. The measurements were made twice to ensure good repeatability of the experiments.[26] Thermal desorption measurements have also been performed with the help of another setup equipped with a thermal conductivity detector and working under continuous Ar flow. Similar results have been obtained by these methods. The onset temperature is defined as the intersection of the tangent of the peak with the extrapolated baseline.

High-Pressure Differential Scanning Calorimetry. High-pressure differential scanning calorimetry (HP-DSC) experiments have been performed under a hydrogen atmosphere using a Setaram Sensys Evo instrument equipped with a high-accuracy 3D Calvet sensor. The samples were loaded without air exposure and heated under hydrogen (0.4 MPa) with a constant temperature ramp (1 $K \cdot min^{-1}$) from 300 to 673 K.

NMR Experiments. Solid-state magic angle spinning (MAS) nuclear magnetic resonance (NMR) spectra were obtained using a Bruker Avance 500 MHz spectrometer. The samples were first diluted using crushed quartz glass powder to avoid

DOI: 10.1021/acs.jpcc.5b05754
J. Phys. Chem. C 2015, 119, 18091−18098

detuning problems from highly electric CT material and packed into 4 mm zirconia rotors inside an Ar glovebox.[27] An airtight Vespel cap was used for variable-temperature measurements, and samples were spun at 8000 Hz using dry N_2 gas. Typically ^{1}H MAS NMR spectra have been recorded at room temperature. In situ ^{1}H MAS NMR experiments have been also performed during heating from room temperature to 473 K. ^{1}H chemical shifts are reported with respect to the tetramethylsilane (TMS) reference.

RESULTS AND DISCUSSION

Structural and Microstructural Properties of MgH_2@CT Composites. XRD patterns of all composites and the pristine carbon template (CT) are displayed in Figure 1.

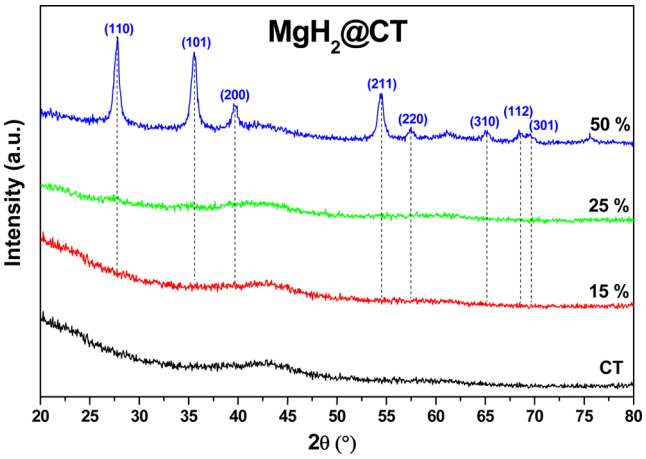

Figure 1. XRD patterns of the pristine carbon template (CT) and composites xMgH$_2$@CT, where x stands for 15, 25, and 50 wt % Mg.

The CT shows a very broad peak at around 43° indicating a low degree of graphitization, in agreement with previous results.[28] For 50MgH$_2$@CT the most intense diffraction peaks originate from the MgH_2 tetragonal phase (JCP no. 01 074 0934). No diffraction peaks from MgH_2 can be noticed for 25MgH$_2$@CT and 15MgH$_2$@CT, suggesting that the MgH_2 nanoparticles have coherence lengths that are too short to diffract X-rays. In the case of 50MgH$_2$@CT, the lattice parameters of MgH_2 nanoparticles are a = 4.510 (8) Å and c = 3.015 (5) Å, in good agreement with the MgH_2 phase,[11] and the average crystallite size is 14(±2) nm, as determined by XRD refinements.

Although XRD showed the presence of crystalline MgH_2 only in the richest Mg composite (50 wt %), TEM investigations confirm the presence of MgH_2 nanoparticles in all composites as evidenced by well-distributed bright spots in the dark-field images (Figure 2). The corresponding particles histograms are also shown, and the statistical average sizes for the three composites are listed in Table 1.

The MgH_2 nanoparticle size distribution strongly depends on the metal content: the majority of the nanoparticles are below 3, 6, and 20 nm for the composites containing 15, 25, and 50 wt % Mg, respectively. The particle distributions are unimodal for 15MgH$_2$@CT and 25MgH$_2$@CT with average sizes of 1.3 and 3.0 nm, respectively. For 50MgH$_2$@CT, the particle size distribution is bimodal with two maxima at 4.5 and 10 nm. Consequently, proposing a statistical average size based on the entire particle size distribution seems to be meaningless. Neither of the two maxima (4.5 and 10 nm) agrees with the crystallite size found from XRD (14 nm). This is not surprising since a similar discrepancy was already encountered for other Mg-based composites.[11] Possibly, only larger MgH_2 nanoparticles contribute to the coherent diffraction of X-rays, as also suggested by the lack of diffraction peaks from 15MgH$_2$@CT and 25MgH$_2$@CT.

It is interesting that, for 15MgH$_2$@CT, the nanoparticle size distribution and the average value match the pore size distribution and average pore size of the pristine carbon (Figure SI-1), suggesting a successful nanoconfinement of MgH_2. For higher Mg content, only small nanoparticles (<2 nm) can be effectively confined in the pores while larger ones are either supported on the external surface or confined in enlarged pores that might have experienced wall expansion and/or structural damage. It is well documented that the formation of metal particles at the external surface is generally accompanied by a large particle size distribution.[29,30]

To discriminate among these hypotheses, N_2 sorption measurements at 77 K have been performed on the MgH$_2$@CT composites before and after metal removal by HCl leaching (Figure SI-3). The textural properties before and after metal removal are listed in Table 1.

The BET specific surface areas and porous volumes of as-synthesized MgH$_2$@CT composites diminish with increasing amounts of Mg. This is mainly due to the increase in the total weight and to the blocking of pores by MgH_2 nanoparticles, as already observed in similar composites.[23,31] The loss of micropore volume (40−57%, from the values relative to the carbon amount) provides more important insights than the decrease in mesoporous volume (8−24%). This suggests that the MgH_2 nanoparticles are preferentially filling the micropores, irrespective of the Mg content.

Figure 3 compares the BET surface area for all as-synthesized composites and the corresponding materials after metal removal. The initial BET surface area is not entirely recovered after HCl treatment. For all composites, the loss of BET surface area varies between 27 and 35%, suggesting irreversible pore damage by the in situ formation and growth of the MgH_2 nanoparticles. Generally, the mesopores volume is increased by nanoparticles embedding, in contrast to the microporous volume. This proves the hypothesis that small MgH_2 nanoparticles are confined in the pores of CT, although the process seems to accompany irreversible pore/structure damage. The loss of structural ordering with Mg loading is also confirmed by X-ray diffraction after acid treatment (Figure SI-4).

Size Effect on Hydrogen Desorption Properties. Hydrogen desorption properties of the MgH$_2$@CT composites have been characterized by two thermal analysis techniques: TDS under vacuum and HP-DSC under a hydrogen atmosphere. The TDS spectra of the three composites are compared to the hydrogen desorption properties of micro-crystalline MgH_2 in Figure 4.

The desorption kinetics from MgH_2 nanoparticles are markedly dependent on the average size: the smaller the size, the lower the temperature of hydrogen desorption. For the smallest nanoparticles with an average size of 1.3 nm (15MgH$_2$@CT), the onset temperature of desorption is around 390 K with two maxima appearing at 490 and 530 K. This TDS profile suggests the presence of two populations of nanoparticles with different desorption kinetics. For MgH_2 nanoparticles with an average size of 3.0 nm (25MgH$_2$@CT), the

DOI: 10.1021/acs.jpcc.5b05754
J. Phys. Chem. C 2015, 119, 18091−18098

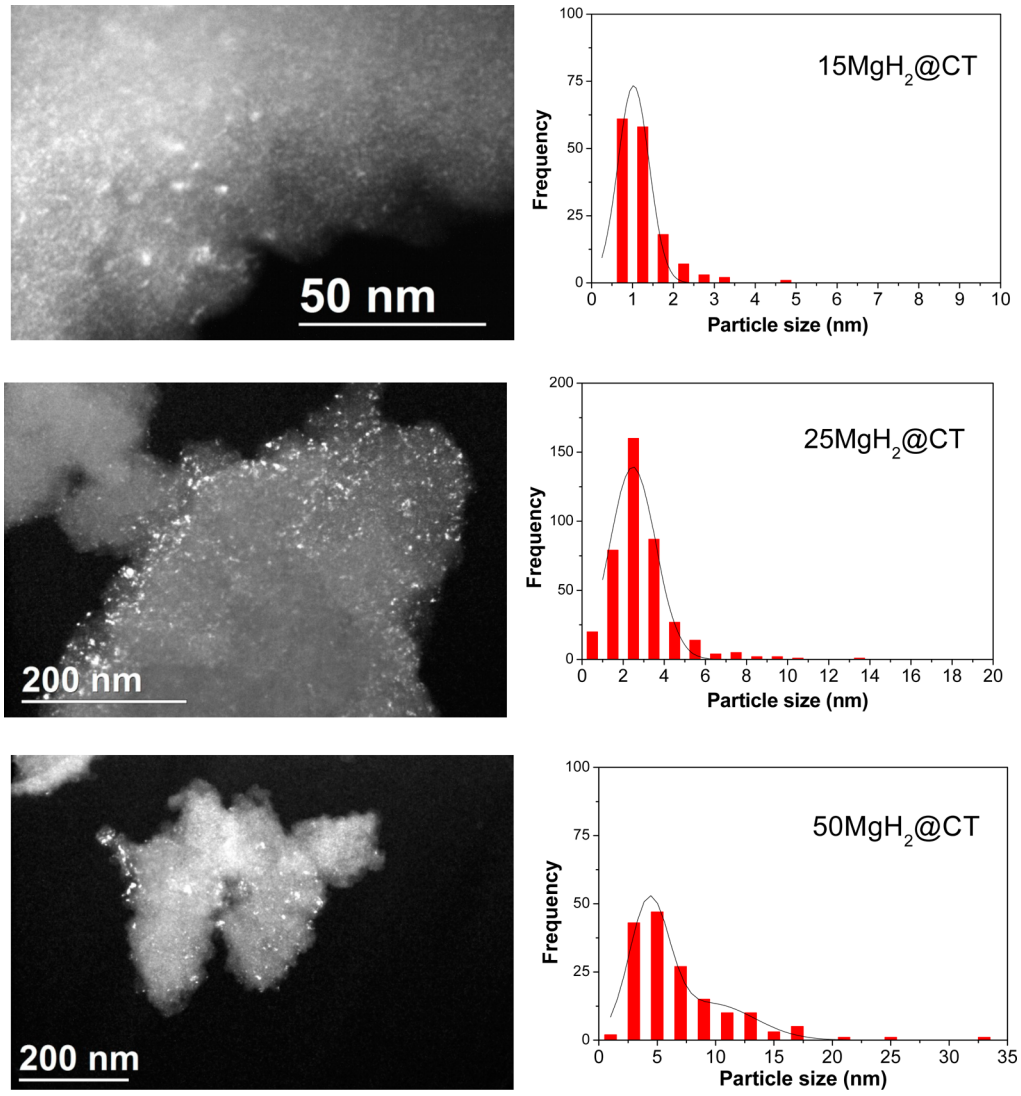

Figure 2. Dark-field TEM images (left) and corresponding MgH_2 nanoparticle size histograms (right) for $15MgH_2$@CT, $25MgH_2$@CT, and $50MgH_2$@CT from top to bottom, respectively.

Table 1. Chemical and Textural Properties (BET Surface Area and Different Porous Volume) of As-Synthesized *x*MgH_2@CT (*x* = 15, 25, and 50 wt % Mg) and after Metal Removal by HCl Leaching[a]

sample	*x* Mg content (wt %)	S_{BET} ($m^2 \cdot g^{-1}$) ± 10	V_{tot} ($cm^3 \cdot g^{-1}$) ± 0.05	V_{micro} ($cm^3 \cdot g^{-1}$) ± 0.05	V_{meso} ($cm^3 \cdot g^{-1}$) ± 0.05	⟨MgH_2⟩ size (nm) XRD	⟨MgH_2⟩ size (nm) TEM
CT		2344	1.54	0.93	0.61		
xMgH_2@CT as-synthesized	15	1252 (1473)	0.89 (1.05)	0.48 (0.56)	0.41 (0.49)		1.3
	25	855 (1140)	0.72 (0.96)	0.30 (0.40)	0.42 (0.56)		3.0
	50	659 (1318)	0.48 (0.96)	0.25 (0.50)	0.23 (0.46)	14	n.d.
xMgH_2@CT after HCl leaching	15	1635	1.33	0.65	0.68		
	25	1751	1.36	0.69	0.67		
	50	1566	1.14	0.60	0.54		

[a]All textural values are given in grams of composite and in parentheses per gram of carbon. The average sizes of MgH_2 nanoparticles for $15MgH_2$@CT and $25MgH_2$@CT are also listed, as determined by TEM. The crystallite average size for $50MgH_2$@CT is given from XRD refinements.

onset temperature of desorption is very close to the previous value and the peak maximum is around 550 K. However, the asymmetric shape of the curve also includes a small desorption peak occurring at lower temperature. This suggests that both $15MgH_2$@CT and $25MgH_2$@CT composites contain two populations of nanoparticles with different desorption kinetics. Generally, this behavior can be explained either by a bimodal particle size distribution or by different interactions with the carbon scaffold. These composites have a unimodal size dispersion according to our TEM results, so the occurrence of two hydrogen desorption peaks is unexpected. Thus, we speculate that different interaction/confinement effect might

DOI: 10.1021/acs.jpcc.5b05754
J. Phys. Chem. C 2015, 119, 18091−18098

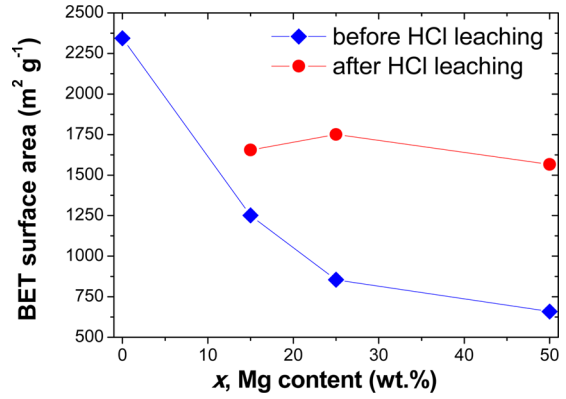

Figure 3. Variation of the BET surface area vs Mg content (wt %) of the xMgH$_2$@CT composites before and after acid leaching. The error bar for the surface area is ±10 $m^2 \cdot g^{-1}$ (Table 1), and it is therefore included in the size of the symbols.

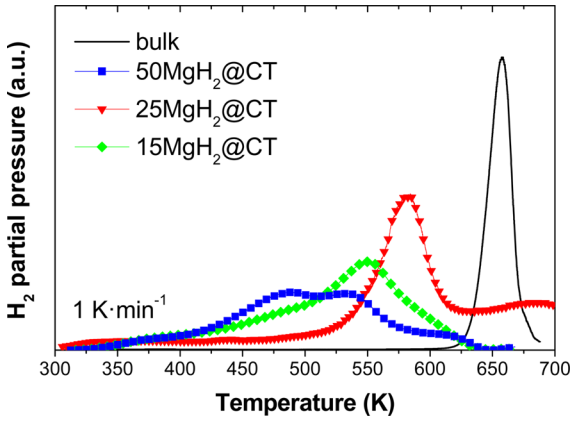

Figure 4. TDS spectra of the xMgH$_2$@CT composites with x = 15, 25, and 50 wt % Mg and bulk MgH$_2$ recorded at a heating rate of 1 K·min^{-1}.

account for this feature. Interestingly, the desorption from both 15MgH$_2$@CT and 25MgH$_2$@CT is completed at 625 K, which is close to the onset temperature of desorption from the bulk state (635 K).

For 50MgH$_2$@CT, the onset temperature of desorption arises at around 525 K, which is 135 K higher relative to the two previous cases. The maximum desorption rate occurs at 580 K, which is still lower than for the bulk sample (657 K). However, this peak is slightly asymmetric, suggesting again two populations of nanoparticles with different desorption kinetics. Moreover, a small shoulder arises at high temperature close to the desorption temperature of bulk MgH$_2$. This might be due to the presence of external bulklike particles. As discussed above, this TDS profile is consistent with the bimodal particle size distribution as shown by the TEM study (Figure 2). The desorption is not completed at 700 K and is attributed to partial desorption from bulklike MgH$_2$ and/or desorption from the carbon scaffold occurring at high temperature.[22]

It is obvious from the TDS results that the hydrogen desorption kinetics of all MgH$_2$@CT composites is noticeably faster than that of bulk MgH$_2$. This can be accounted for by the shorter diffusion length of hydrogen within the nanoparticles, compared to the bulk. The temperature for the maximum desorption rate strongly depends on the average size of the nanoparticles, in agreement with previous studies.[11,16] Moreover, the onset temperature of desorption for MgH$_2$ nanoparticles with sizes below 3.0 nm occurs at a temperature about 245 K lower than for the microcrystalline hydride (390 vs 635 K).

Several thermal desorption analysis methods are employed to obtain the kinetic parameters, such as the activation energy of desorption, E_{des}, a pre-exponential factor, υ, and the order of desorption, n.[32] The most commonly used methods for first-order reactions are Redhead peak's maximum from a single desorption spectrum (eq 1) and Kissinger's method (eq 2[33]) that uses a series of desorption experiments recorded at different heating rates

$$E_{des} = RT_m[\ln(\vartheta/\beta T_m) - 3.46] \quad (1)$$

where T_m is the temperature at the maximum in the desorption peak, R is the universal gas constant, β is the heating rate, and ϑ/β is usually 10^{13} K^{-1}

$$\ln(\beta/T_m^2) = -(E_{des}/RT_m) + \ln k_0 \quad (2)$$

where k_0 is a reaction constant.

The temperature at the maximum in the desorption peak (T_m) shifts with the heating rate (β), and this feature is used by the Kissinger method. Therefore, for the Redhead peak maximum procedure, the choice of the applied heating rate (β) is important for an accurate determination of E_{des}. To estimate the heating rate to be used in the Redhead method, a comparative study between the Redhead and Kissinger methods was conducted on bulk MgH$_2$ (Figure SI-5). The E_{des} value, as obtained by the Kissinger procedure, is 180 kJ·mol^{-1}, in good agreement with previous results for bulk MgH$_2$.[10,34] For the Redhead method, only the value calculated for a heating rate of 1 K·min^{-1} agrees well with the one determined by the Kissinger method. Therefore, it is empirically deduced that the Redhead equation may estimate E_{des} values with reliable accuracy when our desorption experiments are recorded with low heating rates. This methodology has been applied for the determination of E_{des} of the MgH$_2$@CT composites from a single TDS spectrum recorded with 1 K·min^{-1}. For the composite showing two maxima, the more intense peak has been chosen for the application of the Redhead method. Thus, the calculated values of E_{des} are 137, 150, and 160 kJ·mol^{-1} for 15MgH$_2$@CT, 25MgH$_2$@CT, and 50MgH$_2$@CT, respectively. As expected, E_{des} decreases with the decreasing size of MgH$_2$ nanoparticles. This result is in good agreement with the reported diminution of E_{des} from the bulk (195 kJ·mol^{-1}) to 3 nm MgH$_2$ (142.8 kJ·mol^{-1}).[10] Thus, we propose here a simple method based on the Redhead equation for the determination of the activation energy of desorption starting from a single TDS experiment recorded with a low heating rate.

To confirm this size dependence of hydrogen desorption properties, HP-DSC experiments during heating under an H$_2$ atmosphere have been performed. The curves from the 25MgH$_2$@CT and 50MgH$_2$@CT composites and bulk MgH$_2$ are plotted in Figure 5. The calorimetric signal from 15MgH$_2$@CT with the smallest average of the MgH$_2$ nanoparticle size could not be detected.

The HP-DSC measurements show endothermic peaks for all samples typical of hydrogen desorption from metal hydrides. For both composites, two desorption peaks are noticed, confirming that these composites have two nanoparticles populations with different desorption kinetics, in good agreement with the TDS results (see above).

DOI: 10.1021/acs.jpcc.5b05754
J. Phys. Chem. C 2015, 119, 18091−18098

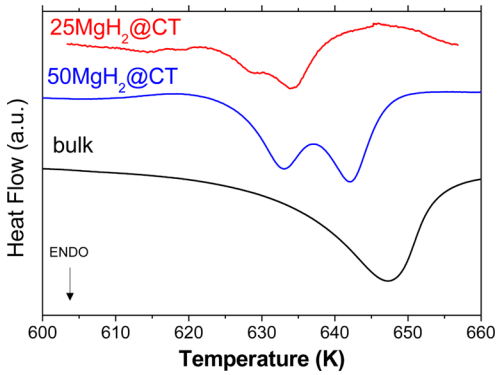

Figure 5. HP-DSC curves for $25MgH_2$@CT, $50MgH_2$@CT, and bulk MgH_2 recorded under 0.4 MPa H_2 pressure with a constant heating rate of 1 K·min^{-1}.

The temperatures of the maximum desorption rate from HP-DSC decrease with the average nanoparticle size from 648 to 633/642 to 629/634 K for the bulk and ca. 20 and 3.0 nm, respectively. This supports the size dependence of the hydrogen desorption properties, as shown by TDS. However, the HP-DSC values are larger than the maxima observed from TDS measurements. Discrepancies between these methods during hydrogen desorption from the same material have already been encountered, with HP-DSC showing a higher peak maximum than TDS.[18] This might be explained by the use of different sample environments (vacuum for the TDS/hydrogen atmosphere for HP-DSC) and detection techniques (H_2 ions directly detected by a mass spectrometer working under vacuum for TDS/difference in the amount of heat required to increase the temperature of the sample vs a reference for HP-DSC). We consider that the most reliable technique is TDS due to the direct measurement of the H_2 desorbed signal by a mass spectrometer under vacuum.

Hydrogen Mobility in MgH_2 Nanoparticles. The hydrogen mobility at room temperature for the $15MgH_2$@CT composite has been determined by ^{1}H MAS NMR spectroscopy and compared to that of bulk MgH_2 (Figure 6).

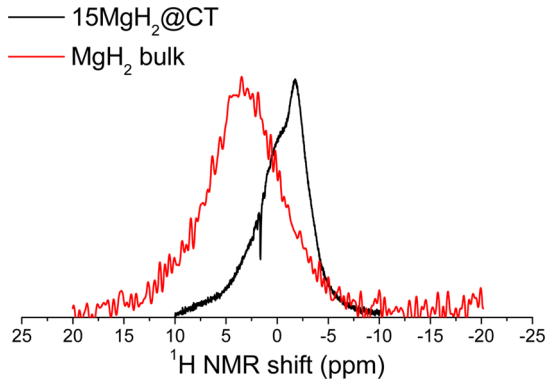

Figure 6. ^{1}H MAS NMR spectra (center band only) from bulk MgH_2 and $15MgH_2$@CT at room temperature.

For the $15MgH_2$@CT composite, two peaks at around 0 and −2 ppm are observed upfield as compared to that for bulk MgH_2 (3 ppm), suggesting two populations of nanoparticles, in agreement with our TDS and HP-DSC results. The upfield peaks might hint at a strong interaction between the MgH_2 nanoparticles and the carbon surface. Moreover, despite additional broadening associated with the presence of the heterogeneous magnetic susceptibility effect of CT surfaces, these upfield peaks are narrower than for the bulk material, which hints at the motional narrowing due to higher hydrogen mobility in nanoparticles than in the bulk, as also reported for similar composites containing MgH_2 nanoparticles supported on a porous carbon (melt infiltration method).[16]

The deconvolution of the signal from $15MgH_2$@CT into two peaks (Figure SI-6) indicates that one part of the nanoparticles (24%) at −2 ppm has a higher hydrogen mobility than the rest of the particles at 0 ppm. This can be understood in the following two hypotheses. The first assumption considers that one part of the MgH_2 particles is effectively nanoconfined, whereas the rest of the particles are present on the external surfaces of carbon. The second hypothesis is based on the core/shell model of particles: the outer shell of nanoconfined particles interacts more strongly with the carbon walls whereas the core of the nanoparticles is less interactive. The latter assumption was recently proposed to explain the enhanced anion mobility of ∼4 nm $LiBH_4$ confined in a porous carbon scaffold.[35] However, it is yet to be further explored which hypothesis can better account for the two desorption peaks noticed in the TDS and HP-DSC curves from the $15MgH_2$@CT composite. A similar description may be applied for the other composites.

The thermal variation of the hydrogen mobility within the $15MgH_2$@CT composite has been determined by in situ ^{1}H MAS NMR spectroscopy during heating from room temperature to 473 K (Figure 7).

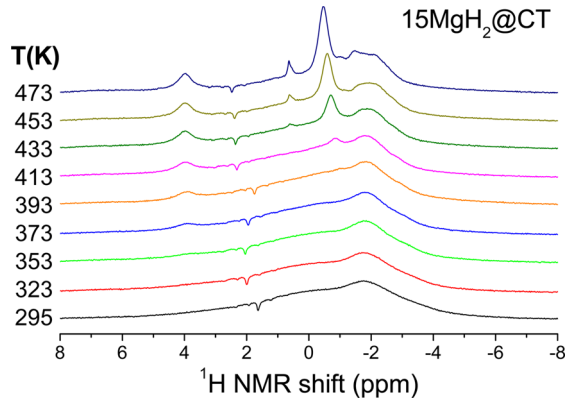

Figure 7. In situ thermal evolution of ^{1}H MAS NMR spectra of the $15MgH_2$@CT composite from 295 to 473 K.

At around 413 K, line narrowing occurs at 0 ppm, which constantly grows with increasing temperature. This indicates higher hydrogen mobility in nanoparticles with increasing temperature. The sharp peak position shifts downfield as the temperature rises. Such low-temperature behavior was never observed for microcrystalline MgH_2, suggesting that this should be caused by the effective nanoconfinement of MgH_2 within the pores of microporous carbon. Moreover, the evolution of H_2 gas at around 4.2 ppm is observed starting at 373 K and increases with increasing temperature. The results indicate hydrogen desorption starting at low temperature, in very good agreement with our TDS result for this composite material. The observed enhanced hydrogen mobility and the increased hydrogen desorption properties of the present MgH_2 nanoparticles appear to be common as nanosize/nanoconfinement

DOI: 10.1021/acs.jpcc.5b05754
J. Phys. Chem. C 2015, 119, 18091−18098

effects and may be closely related to each other as for the properties of all MgH_2@CT composites.

CONCLUSIONS

MgH_2 nanoparticles have been embedded into an ordered microporous carbon. The average nanoparticle size is strongly related to the amount of metal and can be tuned from 1.3 to 3.0 to below 20 nm for 15, 25, and 50 wt % Mg, respectively. Unimodal particle size distributions are obtained for 15 and 25 wt % Mg, whereas a bimodal distribution is noticed for the highest Mg loading. From N_2 sorption measurements, nanoparticles preferentially fill the micropores, although this is accompanied by irreversible micropore damage.

The hydrogen desorption properties are size-dependent, as clearly proven by TDS and HP-DSC techniques. The maximum desorption rate and the activation energy of desorption from nanoparticles are size-dependent: the smaller the particle size, the faster the desorption. The onset temperature of hydrogen desorption for MgH_2 nanoparticles below 3 nm occurs at a temperature about 245 K lower than for the bulk. Two hydrogen desorption peaks are observed for both unimodal composites (15 and 25 wt % Mg).

^1H NMR confirms that hydrogen has a higher mobility within MgH_2 nanoparticles than within microcrystalline MgH_2. Moreover, these investigations suggest two types of MgH_2 nanoparticles with different hydrogen mobilities. This result can be correlated with the two desorption peaks observed by TDS and HP-DSC.

Finally, the short hydrogen diffusion lengths and the enhanced hydrogen mobility within particles may comprehensively explain the increased desorption properties of the present MgH_2@CT composites.

ASSOCIATED CONTENT

Supporting Information

The Supporting Information is available free of charge on the ACS Publications website at DOI: 10.1021/acs.jpcc.5b05754.

Pore size distribution of pristine carbon template CT. Hydrogenation of $MgBu_2$@CT followed by HP-DSC. N_2 sorption measurement at 77 K for all MgH_2@CT composites before and after HCl leaching. X-ray diffraction for pristine CT carbon and the 50MgH_2@CT composite after leaching. Comparative study for the determination of the activation energy of desorption of bulk MgH_2. ^1H MAS NMR spectra for CT and 15MgH_2@CT and related deconvolutions. (PDF)

AUTHOR INFORMATION

Corresponding Author

*E-mail: claudia.zlotea@icmpe.cnrs.fr.

Notes

The authors declare no competing financial interest.

ACKNOWLEDGMENTS

This work was financially supported by the Université Paris-Est Créteil. We acknowledge Julie Bourgon and Eric Leroy for performing TEM measurements and Khaled Bouhlel for valuable help with sample preparation. We thank Peter Bramwell for TPD measurements at Utrecht University. The IEA HIA network is acknowledged for providing opportunities for collaborations and fruitful discussions.

REFERENCES

(1) Zhang, Q.; Uchaker, E.; Candelaria, S. L.; Cao, G. Nanomaterials for Energy Conversion and Storage. *Chem. Soc. Rev.* **2013**, *42*, 3127−3171.

(2) Schuth, F. Encapsulation Strategies in Energy Conversion Materials. *Chem. Mater.* **2014**, *26*, 423−434.

(3) Wagemans, R. W. P.; van Lenthe, J. H.; de Jongh, P. E.; van Dillen, A. J.; de Jong, K. P. Hydrogen Storage in Magnesium Clusters: Quantum Chemical Study. *J. Am. Chem. Soc.* **2005**, *127*, 16675−16680.

(4) Kim, K. C.; Dai, B.; Johnson, J. K.; Sholl, D. S. Assessing Nanoparticle Size Effects on Metal Hydride Thermodynamics Using the Wulff Construction. *Nanotechnology* **2009**, *20*, 204001.

(5) Liang, J. J.; Kung, W. C. P. Confinement of Mg-MgH_2 Systems into Carbon Nanotubes Changes Hydrogen Sorption Energetics. *J. Phys. Chem. B* **2005**, *109*, 17837−17841.

(6) Aguey-Zinsou, K. F.; Ares-Fernandez, J. R. Synthesis of Colloidal Magnesium: A near Room Temperature Store for Hydrogen. *Chem. Mater.* **2008**, *20*, 376−378.

(7) Fichtner, M. Nanoconfinement Effects in Energy Storage Materials. *Phys. Chem. Chem. Phys.* **2011**, *13*, 21186−21195.

(8) Konarova, M.; Tanksale, A.; Norberto Beltramini, J.; Qing, L. G. Effects of Nano-Confinement on the Hydrogen Desorption Properties of MgH_2. *Nano Energy* **2013**, *2*, 98−104.

(9) Paskevicius, M.; Tian, H. Y.; Sheppard, D. A.; Webb, C. J.; Pitt, M. P.; Gray, E. M.; Kirby, N. M.; Buckley, C. E. Magnesium Hydride Formation within Carbon Aerogel. *J. Phys. Chem. C* **2011**, *115*, 1757−1766.

(10) Zhao-Karger, Z.; Hu, J. J.; Roth, A.; Wang, D.; Kubel, C.; Lohstroh, W.; Fichtner, M. Altered Thermodynamic and Kinetic Properties of MgH_2 Infiltrated in Microporous Scaffold. *Chem. Commun.* **2010**, *46*, 8353−8355.

(11) Zlotea, C.; Chevalier-Cesar, C.; Leonel, E.; Leroy, E.; Cuevas, F.; Dibandjo, P.; Vix-Guterl, C.; Martens, T.; Latroche, M. Synthesis of Small Metallic Mg-Based Nanoparticles Confined in Porous Carbon Materials for Hydrogen Sorption. *Faraday Discuss.* **2011**, *151*, 117−131.

(12) De Jongh, P. E.; Allendorf, M.; Vajo, J. J.; Zlotea, C. Nanoconfined Light Metal Hydrides for Reversible Hydrogen Storage. *MRS Bull.* **2013**, *38*, 488−494.

(13) Zlotea, C.; Latroche, M. Role of Nanoconfinement on Hydrogen Sorption Properties of Metal Nanoparticles Hybrids. *Colloids Surf., A* **2013**, *439*, 117−130.

(14) Paskevicius, M.; Sheppard, D. A.; Buckley, C. E. Thermodynamic Changes in Mechanochemically Synthesized Magnesium Hydride Nanoparticles. *J. Am. Chem. Soc.* **2010**, *132*, 5077−5083.

(15) Nielsen, T. K.; Manickam, K.; Hirscher, M.; Besenbacher, F.; Jensen, T. R. Confinement of MgH_2 Nanoclusters within Nanoporous Aerogel Scaffold Materials. *ACS Nano* **2009**, *3*, 3521−3528.

(16) Au, Y. S.; Obbink, M. K.; Srinivasan, S.; Magusin, P. C. M. M.; de Jong, K. P.; de Jongh, P. E. The Size Dependence of Hydrogen Mobility and Sorption Kinetics for Carbon-Supported MgH_2 Particles. *Adv. Funct. Mater.* **2014**, *24*, 3604.

(17) Zhang, S.; Gross, A. F.; Van Atta, S. L.; Lopez, M.; Liu, P.; Ahn, C. C.; Vajo, J. J.; Jensen, C. M. The Synthesis and Hydrogen Storage Properties of a MgH_2 Incorporated Carbon Aerogel Scaffold. *Nanotechnology* **2009**, *20*, 204027.

(18) Zlotea, C.; Cuevas, F.; Andrieux, J.; Ghimbeu, C. M.; Leroy, E.; Léonel, E.; Sengmany, S.; Vix-Guterl, C.; Gadiou, R.; Martens, T.; et al. Tunable Synthesis of (Mg-Ni)-Based Hydrides Nanoconfined in Templated Carbon Studied by in Situ Synchrotron Diffraction. *Nano Energy* **2013**, *2*, 12−20.

(19) Vajeeston, P.; Sartori, S.; Ravindran, P.; Knudsen, K. D.; Hauback, B.; Fjellvåg, H. MgH_2 in Carbon Scaffolds: A Combined Experimental and Theoretical Investigation. *J. Phys. Chem. C* **2012**, *116*, 21139−21147.

(20) Kyotani, T.; Ma, Z.; Tomita, A. Template Synthesis of Novel Porous Carbons Using Various Types of Zeolites. *Carbon* **2003**, *41*, 1451−1459.

DOI: 10.1021/acs.jpcc.5b05754
J. Phys. Chem. C 2015, 119, 18091−18098

(21) Xia, Y.; Yang, Z.; Mokaya, R. Templated Nanoscale Porous Carbons. *Nanoscale* **2010**, *2*, 639−659.
(22) Matei Ghimbeu, C. M.; Guerin, K.; Dubois, M.; Hajjar-Garreau, S.; Vix-Guterl, C. Insights on the Reactivity of Ordered Porous Carbons Exposed to Different Fluorinating Agents and Conditions. *Carbon* **2015**, *84*, 567−583.
(23) Oumellal, Y.; Zlotea, C.; Bastide, S.; Cachet-Vivier, C.; Leonel, E.; Sengmany, S.; Leroy, E.; Aymard, L.; Bonnet, J.-P.; Latroche, M. Bottom-up Preparation of MgH_2 Nanoparticles with Enhanced Cycle Life Stability during Electrochemical Conversion in Li-Ion Batteries. *Nanoscale* **2014**, *6*, 14459−14466.
(24) Cheary, R. W.; Coelho, A. A.; Cline, J. P. Fundamental Parameters Line Profile Fitting in Laboratory Diffractometers. *J. Res. Natl. Inst. Stand. Technol.* **2004**, *109*, 1−25.
(25) Valero-Romero, M. J.; Márquez-Franco, E. M.; Bedia, J.; Rodríguez-Mirasol, J.; Cordero, T. Hierarchical Porous Carbons by Liquid Phase Impregnation of Zeolite Templates with Lignin Solution. *Microporous Mesoporous Mater.* **2014**, *196*, 68−78.
(26) Zlotea, C.; Moretto, P.; Steriotis, T. A Round Robin Characterisation of the Hydrogen Sorption Properties of a Carbon Based Material. *Int. J. Hydrogen Energy* **2009**, *34*, 3044−3057.
(27) Lee, H.-S.; Hwang, S.-J.; Kim, H. K.; Lee, Y.-S.; Park, J.; Yu, J.-S.; Cho, Y. W. In Situ NMR Study on the Interaction between $LiBH_4$−$Ca(BH_4)_2$ and Mesoporous Scaffolds. *J. Phys. Chem. Lett.* **2012**, *3*, 2922−2927.
(28) Kyotani, T.; Ma, Z.; Tomita, A. Template Synthesis of Novel Porous Carbons Using Various Types of Zeolites. *Carbon* **2003**, *41*, 1451−1459.
(29) Munnik, P.; Velthoen, M. E. Z.; de Jongh, P. E.; de Jong, K. P.; Gommes, C. J. Nanoparticle Growth in Supported Nickel Catalysts during Methanation Reaction—Larger Is Better. *Angew. Chem.* **2014**, *126*, 9647−9651.
(30) Rosler, C.; Fischer, R. A. Metal-Organic Frameworks as Hosts for Nanoparticles. *CrystEngComm* **2015**, *17*, 199−217.
(31) de Jongh, P. E.; Wagemans, R. W. P.; Eggenhuisen, T. M.; Dauvillier, B. S.; Radstake, P. B.; Meeldijk, J. D.; Geus, J. W.; de Jong, K. P. The Preparation of Carbon-Supported Magnesium Nanoparticles Using Melt Infiltration. *Chem. Mater.* **2007**, *19*, 6052−6057.
(32) Dejong, A.; Niemantsverdriet, J. Thermal Desorption Anaylsis: Comparative Test of Ten Commonly Applied Procedures. *Surf. Sci.* **1990**, *233*, 355−365.
(33) Blaine, R. L.; Kissinger, H. E. Homer Kissinger and the Kissinger Equation. *Thermochim. Acta* **2012**, *540*, 1−6.
(34) Zlotea, C.; Sahlberg, M.; Ozbilen, S.; Moretto, P.; Andersson, Y. Hydrogen Desorption Studies of the $Mg_{24}Y_5$-H System: Formation of Mg Tubes, Kinetics and Cycling Effects. *Acta Mater.* **2008**, *56*, 2421−2428.
(35) Liu, X.; Majzoub, E. H.; Stavila, V.; Bhakta, R. K.; Allendorf, M. D.; Shane, D. T.; Conradi, M. S.; Verdal, N.; Udovic, T. J.; Hwang, S.-J. Probing the Unusual Anion Mobility of $LiBH_4$ Confined in Highly Ordered Nanoporous Carbon Frameworks via Solid State NMR and Quasielastic Neutron Scattering. *J. Mater. Chem. A* **2013**, *1*, 9935−9941.

DOI: 10.1021/acs.jpcc.5b05754
J. Phys. Chem. C 2015, 119, 18091−18098